



Publication Year	2017
Acceptance in OA	2021-02-02T14:30:29Z
Title	Electrostatic analyzer design for solar wind proton measurements with high temporal, energy, and angular resolutions
Authors	Cara, Antoine, Lavraud, Benoit, Fedorov, Andrei, De Keyser, Johan, DE MARCO, Rossana, MARCUCCI, Maria Federica, VALENTINI, FRANCESCO, SERVIDIO, SERGIO, BRUNO, Roberto
Publisher's version (DOI)	10.1002/2016JA023269
Handle	http://hdl.handle.net/20.500.12386/30163
Journal	JOURNAL OF GEOPHYSICAL RESEARCH. SPACE PHYSICS
Volume	122

1
2
3 **Electrostatic analyzer design for solar wind proton measurements with high**
4 **temporal, energy and angular resolutions**
5
6

7 **Antoine Cara^{1,2}, Benoit Lavraud^{1,2}, Andrei Fedorov^{1,2}, Johan De Keyser³, Rossana**
8 **DeMarco⁴, M. Federica Marcucci⁴, Francesco Valentini⁵, Sergio Servidio⁵, and Roberto**
9 **Bruno⁴**

10 ¹ Institut de Recherche en Astrophysique et Planétologie, Université de Toulouse, France

11 ² Centre National de la Recherche Scientifique, UMR 5277, Toulouse, France

12 ³ IASB - BIRA, Brussels, Belgium

13 ⁴ INAF – IAPS, Rome, Italy

14 ⁵ Dipartimento di Fisica, Università della Calabria, Rende (CS), Italy

15
16
17
18 Corresponding author:

19 A. Cara, Institut de Recherche en Astrophysique et Planétologie, 9 avenue du colonel Roche, BP
20 44346, 31028 Toulouse Cedex 4, France. (Antoine.Cara@irap.omp.eu)

21
22
23
24 Key Points:

- 25 • A new solar wind ion instrument design is presented
- 26 • Simulations are used to define a design which permits unprecedented temporal and angular
27 resolutions
- 28 • A plasma turbulence simulation is used to show the measurement capabilities achieved
29
30

31

32

33 Abstract

34 We present the design study of an electrostatic analyzer that permits combined high temporal,
35 energy and angular resolution measurements of solar wind ions. The requirements for high
36 temporal, energy and angular resolutions, combined with the need for sufficient counting statistics,
37 leads to an electrostatic analyzer with large radius (140 mm) and large geometric factor. The
38 resulting high count rates require the use of Channel Electron Multipliers (CEMs), instead of
39 Micro-Channel Plates (MCPs), to avoid saturation. The large radius further permits the placement
40 of 32 CEM detectors at the analyzer focal plane, thereby providing very high angular resolution in
41 azimuth (1.5°). Electrostatic simulations were performed to define the analyzer geometric factor,
42 energy resolution, analyzer constant (K), elevation response, etc. Simulations were also performed
43 to define the geometry of the deflectors and collimator that are used to provide the proper energy
44 resolution, field-of-view and angular resolution (1.5°) in elevation as well (the total field-of-view
45 of the design is $\pm 24^\circ \times \pm 24^\circ$). We show how this design permits unprecedented measurements of
46 the fine structure of the solar wind proton beam and other important features such as temperature
47 anisotropy. This design is used for the Cold Solar Wind (CSW) instrument of the medium-class
48 Turbulent Heating ObserveR (THOR) mission, currently in phase A at the European Space
49 Agency. These unprecedented measurement capabilities are in accordance with and even beyond
50 the requirements of the mission.

51

52 1. Introduction

53 1.1 Upcoming missions and science objectives

54 Current space missions such as WIND [*Lin et al.*, 1995], ACE [*McComas et al.*, 1998] or
55 Cluster [*Rème et al.*, 2001], typically perform in situ ion measurements in space with rather low
56 temporal (few seconds at best) and angular resolutions ($\sim 3^\circ$ at best). While such properties are
57 sufficient for numerous purposes, they are far from being sufficient for the study of kinetic-scale
58 processes associated with turbulence, shocks and reconnection, in particular in the solar wind
59 [e.g., *Schwartz et al.*, 2009 ; *Bruno and Carbone*, 2013]. The requirement for high energy and
60 angular resolutions comes, on the one hand, from the basic property of solar wind proton
61 distribution functions that have the form of a cold beam with only a small angular width.
62 Typically, it can be described by a drifting bi-Maxwellian (with a noticeable temperature
63 anisotropy), but it often manifests more complex shapes [e.g., *Bruno and Carbone*, 2013]. Such
64 non-Maxwellian features indicate the presence of fundamental kinetic plasma instabilities that,
65 together with turbulence, are crucial for understanding the dynamics of the interplanetary medium
66 [e.g., *Marsch*, 2006]. The requirement for high time resolution comes, on the other hand, from the
67 fact that (1) the solar wind flows very fast past the spacecraft, leaving little time to sample solar
68 wind structures such as thin current sheets, and (2) that the typical growth time of ion instabilities
69 in the solar wind is on the order of few cyclotron periods [*Montgomery et al.*, 1975]. A good
70 understanding of wave-particle interactions can thus only be obtained if the growing phase of
71 instability is observed, i.e., several observations of the full 3-D velocity distribution function are
72 required during the development of the instability itself.

73
74
75
76
77
78
79
80
81
82
83
84
85
86
87
88
89
90
91
92
93
94
95
96
97
98
99
100
101
102
103
104
105
106
107
108
109
110
111
112
113
114
115

Solar wind ion measurements are currently being performed, for example, by Cluster (*Rème et al. [2001]*), ACE [*McComas et al., 1998*] and WIND (*Ogilvie et al. [1995]*). Such measurements will be performed with enhanced capabilities on future missions such as Solar Orbiter (Proton and Alpha Sensor; PAS) and Solar Probe Plus (Solar Probe Analyzer; SPAN; *Kasper et al. [2016]*). The properties of these instruments are shown in Table 1. However, as presented here and in the companion paper [*DeMarco et al., 2016*], the study of kinetic-scale processes in the solar wind (turbulence, etc.) requires much more detailed measurements of the solar wind proton distribution function. Note also that despite a high time resolution (150 ms), the ion instrument Magnetospheric Multiscale (MMS) [*Pollock et al., 2016*] mission is not designed for fine measurements of the proton beam in the solar wind, owing to a 11.25° angular resolution.

The THOR (Turbulent Heating Observer) mission [*Vaivads et al., 2016; <http://thor.irfu.se/>*], which is currently in phase A as a medium-class M4 mission within the science programme of the European Space Agency, is designed to address turbulent energy dissipation and particle energization in the interplanetary plasma, in different physical regimes and different regions (Earth's bow shock and magnetosheath, foreshock, undisturbed solar wind and interplanetary shocks). To maximize the time spent in the key target regions, the THOR orbit is close to the ecliptic plane with a three science phases. Each phase has a different orbit and a term of one year. The first year is dedicated to magnetosheath and bow shock studies with an apogee of $16 R_E$ (Earth radii). The second phase targets the solar wind, shock and foreshock with an apogee of $26 R_E$. The third phase will focus on the pristine solar wind and interplanetary shocks with an apogee of $60 R_E$. Here we present the work that has been performed to design the Cold Solar Wind (CSW) instrument of the THOR mission, which is dedicated to the measurement of the solar wind proton beam with unprecedented temporal (150 ms) and angular (1.5°) resolutions. CSW will measure the three-dimensional distribution function of solar wind ions in the range 20 eV – 20 keV. In certain modes with a large energy range it will also measure alphas. To ensure high temporal resolution and continuous measurements of the solar wind ion beam, the CSW instrument is accommodated on the side of the spacecraft with a field-of-view centered on the Sun direction and aligned with the spacecraft spin axis. Moreover, the high angular resolution (down to 1.5°) requires a slow spacecraft spin rate (2 rpm is planned for the THOR spacecraft).

Table 1 lists the basic properties of some solar wind instruments in comparison to the properties of the design reported here for CSW on THOR. The values given for CSW in the Table are the measurement requirements that ensue from the science requirements of the mission (<http://thor.irfu.se/>). Between parentheses we give the actual characteristics planned for the CSW instrument on the basis of the present study. The proposed increase in angular resolution in particular will strongly benefit the science return of the mission as shown in Section 3 and in the *DeMarco et al. [2016]*.

116
117
118
119
120

Table 1. Main properties of a few past and future solar wind instruments (for full distribution function measurement).
TOF: Time-of-flight.

	Cluster (HIA)	Solar Orbiter (PAS)	Solar Probe plus (SPAN)	THOR (CSW)
Type of instrument	ESA + MCP	Deflector + ESA + CEM	Deflector + ESA + MCP + TOF	Deflector + ESA + CEM
Spacecraft spin and FOV	15 rpm Spin axis orthogonal to FOV	3-axis stabilized	3-axis stabilized	2 rpm Spin axis aligned with FOV
3D sampling time resolution	4s	1s	3.5s	150ms
Full energy range	5 eV – 32 keV	200 eV – 20 keV	5 eV – 30 keV	200 eV – 20 keV (20 eV – 20 keV)
Energy resolution $\Delta E/E$	18%	$\sim 7\%$	7%	5% - 8% (7%)
Azimuth resolution	5.6°	6°	11.25°	3° (1.5°)
Elevation resolution	5.6°	5°	5°	3° (1.5°)
Azimuth range	360°	-24° + 42°	240°	$\pm 24^\circ$
Elevation range	$\pm 180^\circ$	$\pm 22.5^\circ$	$\pm 60^\circ$	$\pm 24^\circ$
Sphere radius	40.2 mm	72.5 mm	~ 35 mm	140 mm
Geometric Factor (total) [$cm^2 \cdot sr \cdot keV/keV$]	$1.9 \cdot 10^{-4}$ (one half) $4.9 \cdot 10^{-3}$ (other half)	$4.4 \cdot 10^{-5}$ (11 anodes)	Not known	$7 \cdot 10^{-4}$ (32 anodes)

121
122

1.2 Basic instrument design

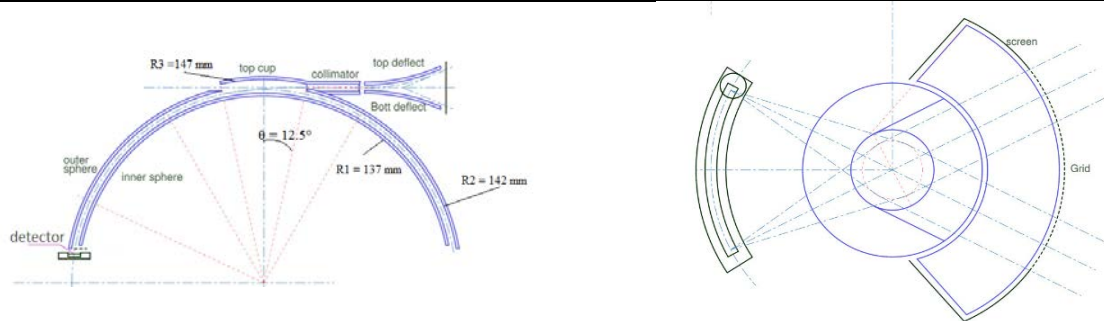
123 The designs most frequently used for solar wind ion measurements are based on Faraday
124 cups (FC) or electrostatic analyzers (ESA) coupled with detectors. Faraday cups are composed of
125 a cup with grids and two semicircular collector plates. The grids are polarized to select incident
126 particles by energy (as a retarding potential analyzer) and the particle flux is estimated through the
127 measurement of the current on each collector. ESAs select incident particles by deflecting them
128 with an electrostatic field applied between concentric plates. Only particles within the appropriate
129 energy range are able to reach detectors placed at the exit of the analyzer (channel electron
130 multipliers or micro-channel plates). ESAs are often coupled with deflector systems at their
131 entrance in order to measure out of the natural analyzer detection plane. All these aspects are
132 further detailed in the next sections.

133 The spectrometer used for CSW is based on a top-hat electrostatic analyzer design [*Carlson*
134 *and McFadden*, 1982], which is composed of two concentric hemispheric plates for ion energy-
135 per-charge selection. Such a design permits fine focusing onto the detectors at the ESA exit, in
136 accordance with the requirement for high angular resolution measurements (right-hand side of
137 Figure 1). The outer hemisphere potential is set to ground while the inner sphere potential varies
138 according to the particle energy-per-charge to measure (left-hand side of Figure 1). The elevation
139 angle selection is performed thanks to high voltages applied on deflector plates at the entrance of

140 the analyzer which allows a fast 3D measurement (e.g., Solar Orbiter or Solar Probe Plus, Table
141 1). A collimator is used between the deflectors and the top-hat entrance to ensure the required
142 energy and angular (in elevation) resolutions, while the azimuthal resolution (right-hand side of
143 Figure 1) is obtained through appropriate sectorization of the detectors and anodes.

144 In section 2, we present the design of the electrostatic optics and detectors, focusing first
145 on the ESA and collimator that will define the energy, elevation, and azimuth response of the
146 instrument. The study then focusses on the design of the deflectors. The final design performance
147 characteristics are presented in section 3.

148



149 Figure 1. Two-dimensional schematics of (a) analyzer electrostatic design and (b) typical top-hat focusing properties.

150

151 2. Electrostatic optics design

152 2.1 Electrostatic analyzer

153 In this section, the ESA and collimator only are considered to characterize the energy,
154 elevation and azimuth response that correspond to the needs of the instrument.

155

156 2.1.1 Geometric design

157 As mentioned in Table 1, the baseline 3D ion distribution sampling time for THOR/CSW
158 is 150 ms. Yet the accumulated counts per elementary 3D distribution bin must be high enough to
159 ensure sufficient statistical significance of the data, as further addressed in section 3. The
160 requirement for high counting statistics, combined with the required high time resolution, means
161 that the detectors used at the ESA exit must have a high count rate saturation threshold.

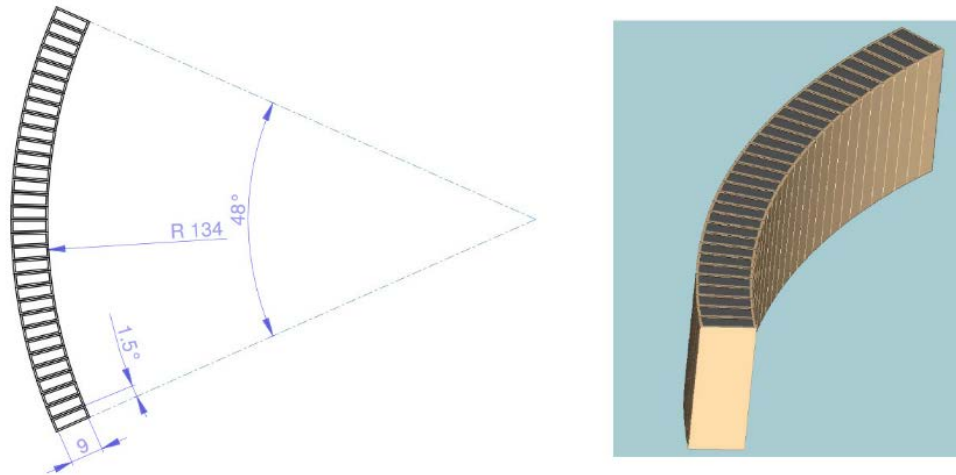
162 MCP (Micro Channel Plate) detectors typically saturate at $1\,000\,000\text{ count s}^{-1}\text{ cm}^{-2}$. Basic
163 calculations show that for an electrostatic analyzer of radius 14 cm with an energy resolution of
164 7% (the basic properties of the instrument as determined through the analysis performed in the
165 next sections), MCPs with an anode size of 3° would lead to saturation for any counting statistics
166 above 500 counts in a baseline 1 ms elementary accumulation time. What this basic calculation
167 shows is that MCPs are not appropriate for such high count rate requirements. The baseline design
168 thus uses Channel Electron Multipliers (CEMs) instead of MCPs as detectors. The advantages are
169 two-fold: (1) CEM count rate saturation is around 10^7 count/s , a factor 10 above MCPs, and (2)
170 this saturation is typical for one CEM, rather than for “an area”, as for MCPs.

171

172

173

174 For these reasons, we further decide to use 32 CEMs (Figure 2) with a resolution of 1.5°
175 each in azimuth for a total $\pm 24^\circ$ field-of-view (FOV). With this design, we can use the full
176 geometric factor of the analyzer, decrease the chance of saturation by a factor 2, and increase the
177 angular resolution up to 1.5° in azimuth. As demonstrated in section 3, with this design we will
178 need to perform angular bin summations (2 elevations \times 2 azimuths) to increase statistics only in
179 cases of tenuous solar wind. The baseline characteristics of the CSW design, which are further
180 studied in the next sections, are summarized in Table 1.



181

182 Figure 2. Basic geometry of the CEM detector array that will be used for CSW on THOR. (a) Basic dimensions of
183 the array, and (b) its 3D rendering.

184

185

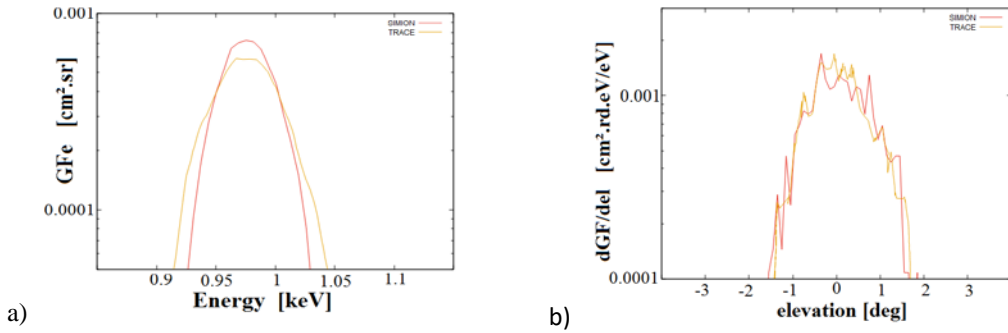
186 2.1.2 Analyzer characterization

187 The electrostatic analyzer introduced above has been studied in detail through simulations
188 using two separate software packages (Simion (<http://www.simion.com>) and Trace (software
189 developed at IRAP)) for thorough benchmarking.

190 These simulations consist in calculating the electrostatic potential around and inside the
191 analyzer mechanical model using finite differences for Simion and finite element methods for
192 Trace. A particle beam is launched upstream of the ESA aperture. The particle source used here is
193 a rectangle, uniformly distributed in position, energy and elevation, while the azimuth for all
194 particles is 0° , as introduced by *Collinson* [2012]. The electrostatic analyzer responses are obtained
195 by studying the energy, elevation and position of the transmitted particles.

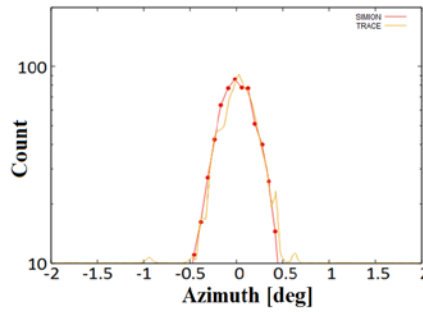
196 The analyzer energy and elevation responses calculated through simulation are plotted in
197 Figure 3 for an analyzer inner plate voltage of 71.5 V. The two curves show the results with Simion
198 (red) and Trace (yellow). Both give similar results. The energy response shows that the analyzer
199 constant K (which relates the energy bandpass to the voltage applied to the analyzer) is 13.8 with
200 an energy resolution of 7%. The elevation response shows a peak in transmission for zero elevation

201 angle with a resolution of about 1.7° . All of these values are in agreement with the scientific
 202 requirements of the THOR mission for high angular and energy resolution, as given in Table 1.
 203



204 Figure 3. Energy (a) and elevation (b) response obtained with 2 different codes, Simion (red) and Trace (yellow).
 205

206 The azimuth response is obtained by measuring the angular position of the particles on the
 207 detectors, after selection and focusing through the electrostatic analyzer. The results obtained by
 208 the two codes for the present ESA characteristics are presented in Figure 4. The simulations show
 209 an azimuth angular resolution below 1° , thus well consistent with the scientific requirements as
 210 well (cf. Table 1).



211
 212 Figure 4. Azimuth analyzer response obtained with 2 different codes, Simion (red) and Trace (yellow).
 213

213 2.1.3 Geometric factor

214 The last but not the least key parameter that needs to be determined is the analyzer
 215 transmission rate or Geometric Factor (GF). This factor relates the count rate measured to the
 216 incident ion energy flux:

$$217 C_{in} = \mathbb{G} F_E \cdot J_E \quad (2.1)$$

218 This factor is estimated with the method introduced by *Collinson* [2012] (without taking
 219 into account the detector efficiency). The formula is given in Eq. (2.2), where C_{ijk} is the number
 220 of particles which strike the simulated detector, $\Delta Y_b \times \Delta Z_b$ is the rectangle area over which
 221 particles are launched, $\overline{E_b}$ and $\overline{\theta_b}$ are the average incident particle energy and elevation, ΔE_b and
 222 $\Delta \theta_b$ are the energy and elevation range of the particle source, $\Delta \varphi$ is the angular width of the anodes,
 223 E_0 is the peak of the energy acceptance and N_{in} the number of incident particles launched. For a
 224 3° azimuthal bin, this factor is about:

$$225 \mathbb{G} F_{3\text{deg}} = \frac{C_{ijk} \Delta Y_b \Delta Z_b \overline{E_b} \Delta E_b \Delta \theta_b \cos^2 \overline{\theta_b} \Delta \varphi}{E_0^2 N_{in}} = 4.4 \times 10^{-5} \text{cm}^2 \cdot \text{sr} \cdot \text{eV/eV} \quad (2.2)$$

226

227

228 This analyzer thus largely responds to the scientific requirements of the THOR mission
229 with an energy resolution around 7%, an elevation resolution below 1.7° and a resolution in
230 azimuth below 1° . As will be shown later using actual expected solar wind ion fluxes to estimate
231 the counting statistics, these numbers (and the GF in particular) are also compatible with the
232 proposed increase in elevation and azimuthal angular resolutions to 1.5° .

233

234 2.2 Electrostatic deflection

235 In addition to the $\pm 24^\circ$ FOV defined by the 32 CEMs of 1.5° each in the azimuthal plane,
236 the measurement of the 3D ion distribution function is performed through the use of electrostatic
237 deflectors at the entrance of the analyzer to steer the look direction in the elevation direction as
238 well. This is done by applying appropriate voltages to the deflectors, whose geometry has been
239 optimized to permit a FOV of $\pm 24^\circ$ in elevation (as for the azimuth FOV). A D -factor can be
240 defined (D in Eq. 2.3). It relates the peak elevation (El) bandpass to the deflector voltages ($U_{def} =$
241 $U_{d1} - U_{d2}$) which define the deflector efficiency:

242

$$(El - El_0) = D \frac{U_{d1} - U_{d2}}{E/q} = \frac{D}{K} \frac{U_{d1} - U_{d2}}{U_{an}} = \frac{D}{K} \frac{U_{def}}{U_{an}} \quad (2.3)$$

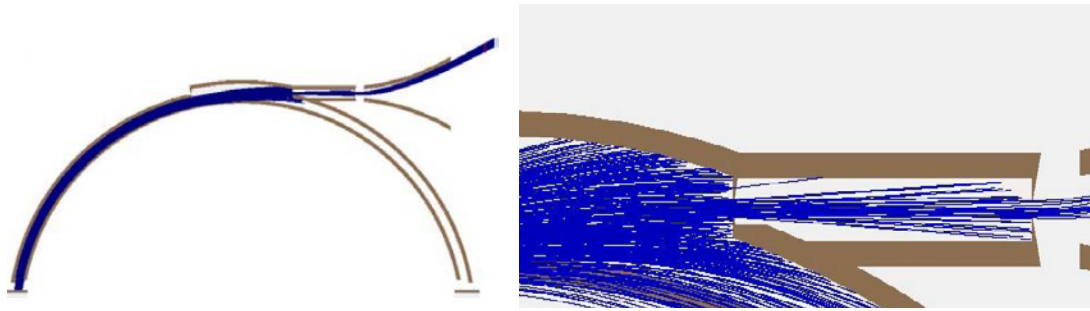
243 where q is the elementary electron charge and E the measured particle energy, which is directly
244 related to the analyzer voltage (U_{an}) through the analyzer constant K .

245

246 2.2.1 Deflector Design

247 Designing the deflection system consists in finding the best trade-off between deflection
248 efficiency and elevation bandpass. The inter-deflector distance defines the elevation range and
249 thus must be large enough to measure particles within the desired elevation bandpass without a
250 decrease in geometric factor (due to mechanical blocking of the particle trajectories). But, on the
251 other hand, to obtain a high efficiency the deflectors must be sufficiently close so as to provide the
252 highest electrostatic field (and thus deflect particles) with minimal applied voltages.

253 Simulations have been performed to find the minimum inter-deflector distance that respects
254 the scientific requirements of the instrument, by calculating the ion trajectories from the detector
255 to the deflectors and determining the associated maximal elevation of the incoming particles. With
256 the design displayed in Figures 1 and 5a, the decrease in geometric factor only appears for
257 elevations around 30° , as discussed later on the basis of Figure 9a. The design is thus appropriate
258 to measure particles within the desired elevation range, with appropriate margins compared to the
259 baseline FOV ($\pm 24^\circ$). Note that the collimator, which is made of two blade-shaped collimators,
260 also plays a key role in determining the elevation and energy resolutions, as illustrated with particle
261 tracing in Figure 5b.

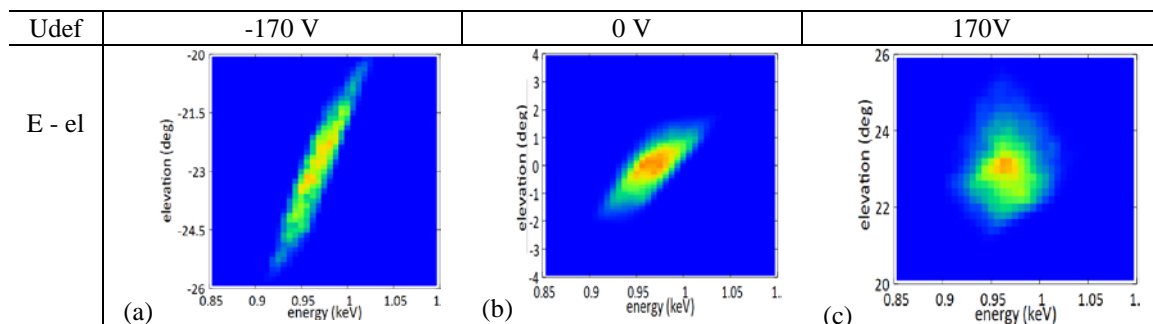


262 Figure 5. (a) Actual design with sample particle tracing (particles are launched from the detectors on the bottom-left-
 263 hand side), and (b) zoom-in on the collimator area to highlight its importance in determining the elevation of accepted
 264 particles, and in turn elevation and energy resolutions.
 265

266 2.2.2 Deflector Characterization

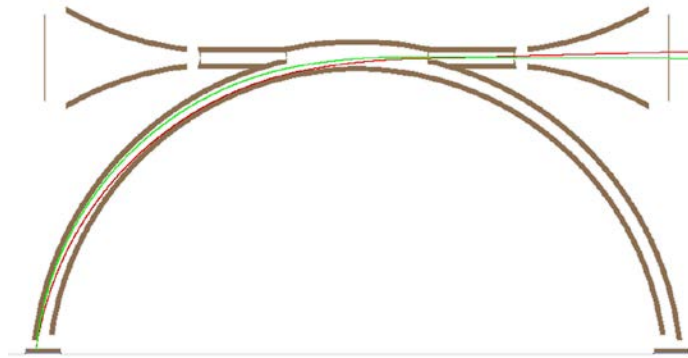
267 The first purpose of simulations is to determine the deflector efficiency (through the D -
 268 factor) and thus the maximum voltage to apply between the deflectors to get the required elevation
 269 range. The analyzer potential applied here is -71.5 V to select particles with an energy around 1
 270 keV and deflector voltages are varied. Figure 6 shows the energy-elevation response for different
 271 elevations/voltages.

272 The observed oval shape of the energy-elevation response for no deflection (central plot
 273 in Figure 6) corresponds to the typical response of an electrostatic analyzer without deflectors at
 274 the entrance. The fact that this transmission function favors slightly higher energy particles for
 275 positive elevations, and conversely lower energy particles for negative elevations, is a classical
 276 property of a top-hat analyzer [e.g., *Carlson and McFadden*, 1998]. It merely reflects the fact that
 277 given the finite separation of the analyzer hemispheric plates, particles coming from positive
 278 elevation can only go through the entire analyzer if they have a slightly higher energy (than the
 279 average energy) and radius of curvature. Similarly, only slightly lower energy particles can go
 280 through if coming from negative elevations. This fact is illustrated in Figure 7. As can be seen in
 281 Figure 6a and 6b, the deflection system exacerbates this effect (oval shape) for negative elevation
 282 steering, while it decreases it for positive steering. This pure electrostatic optics effect results in a
 283 slightly lower angular resolution for negative elevations (1.7° FWHM as noted previously), but
 284 which remains consistent with the science requirements.
 285



286 Figure 6. Response function calculated with SIMION showing the transmission rate over the energy and elevation
 287 response for three deflector potentials considered: (a) $U_{def} = -170$ V, (b) 0 V and (c) 170 V. For this simulation both
 288 deflectors are polarized in an anti-symmetrical fashion.
 289

290



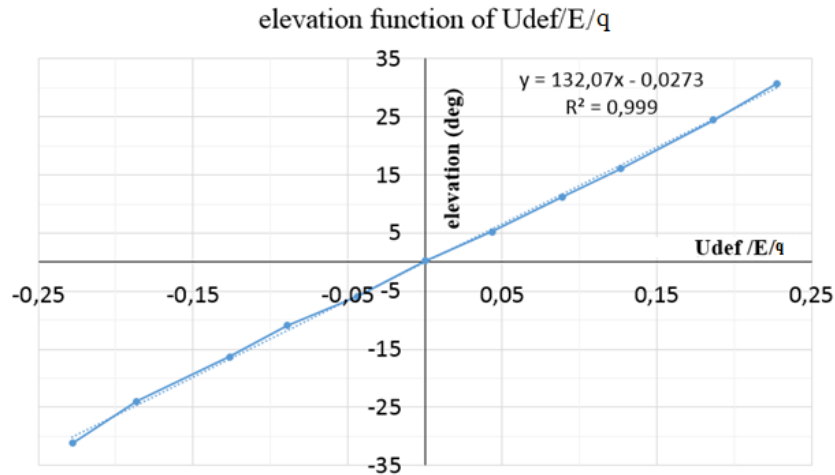
291

292 Figure 7. Typical trajectories plotted for two particles: high energy (red) and low energy (green).

293

294 Figure 8 illustrated the relation between the deflection angle and the deflector voltage, which can be approximated by a linear function with a constant D equal in the present design to $132^\circ \cdot V/V$. Therefore, to detect particles with an energy around 20 keV and an elevation of about 25° , the high voltage circuit must provide a voltage of 3.8 kV for the deflectors (or ± 1900 V).

298



299

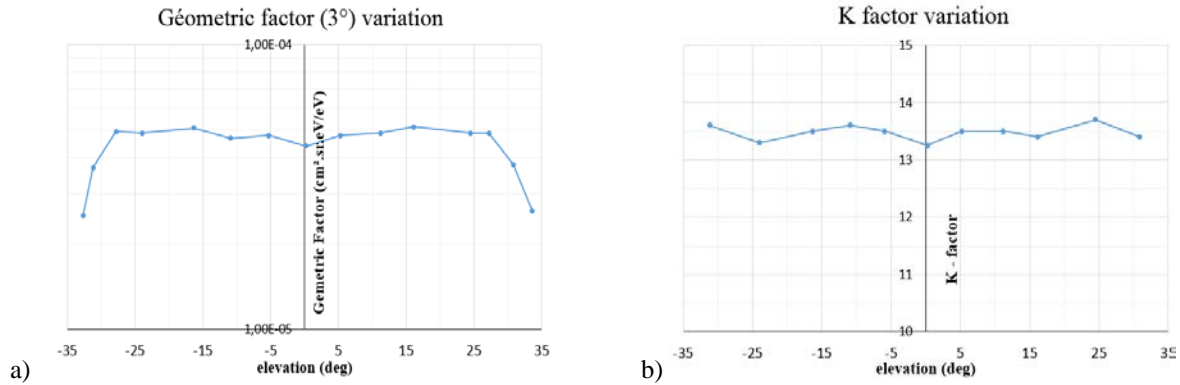
300 Figure 8. Deflection angle as a function of deflector potentials (per energy per charge).

301

302 2.2.3 Performance variation with deflection

303 Finally, the variation of the analyzer performance with deflection is analyzed. Figure 9 shows the variation of the transmission rate (GF) and analyzer constant K . These are constant for all elevations, as required per Liouville's theorem and electrostatic optics. It shows that the deflector geometry is appropriate and no blocking of particle trajectories occurs for the proposed design.

308

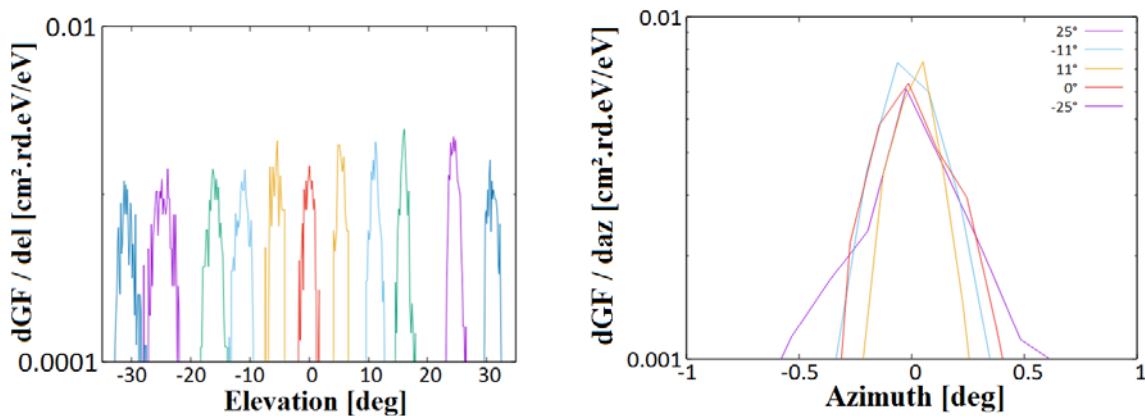


309 Figure 9. GF (a) and K-factor (b) variation as a function of the elevation angle.

310

311 Figure 10 shows the elevation and azimuth responses of this instrument design for different
 312 deflector potentials. The center elevation shifts as expected, as a function of the deflector voltage.
 313 However, we note a small degradation, as mentioned in section 2.2.2, of the elevation resolution
 314 for negative deflections. The azimuth response, on the other hand, shows little variation due to the
 315 deflectors, despite a small change in the focal length of the electrostatic analyzer. This is not an
 316 issue, however, as we do not want a drastic focusing anyway, in order to mitigate the fact that there
 317 is a dead zone between each CEM (~20%). This slight defocusing (yet within ~1° resolution)
 318 should indeed permit a smoother response across all CEMs. Despite the slightly degraded elevation
 319 resolution at negative elevations, all characteristics satisfy the scientific requirements of the
 320 mission.

321



322 Figure 10. Elevation (a) and azimuth (b) response of the design.

323

324 3. Scientific performance and measurement scheme

325 The scientific goal of the present design is to measure the full 3D distribution function of
 326 solar wind protons at 1 AU (and alphas, but these are left for future work) in unprecedented details.
 327 The objective of this section is to determine the impact of the instrument basic accumulation time
 328 and angular resolution (1.5° or 3°) on the statistics of each elementary measurement (counts) given
 329 the Geometric Factor of the proposed design.

330

331 3.1 Basic solar wind modeling

332 As presented in section 2.2, the current design has a GF of $4.4 \times 10^{-5} \text{ cm}^2 \cdot \text{sr} \cdot \text{eV}/\text{eV}$ for 3°
 333 resolution in azimuth. However, to ensure that both the statistics is sufficient and that the CEM
 334 detectors do not saturate, an additional study must be done taking into account known fluxes of
 335 solar wind protons at 1 AU. For that purpose, the distribution function of the solar wind proton
 336 beam is approximated as a drifting Maxwellian:

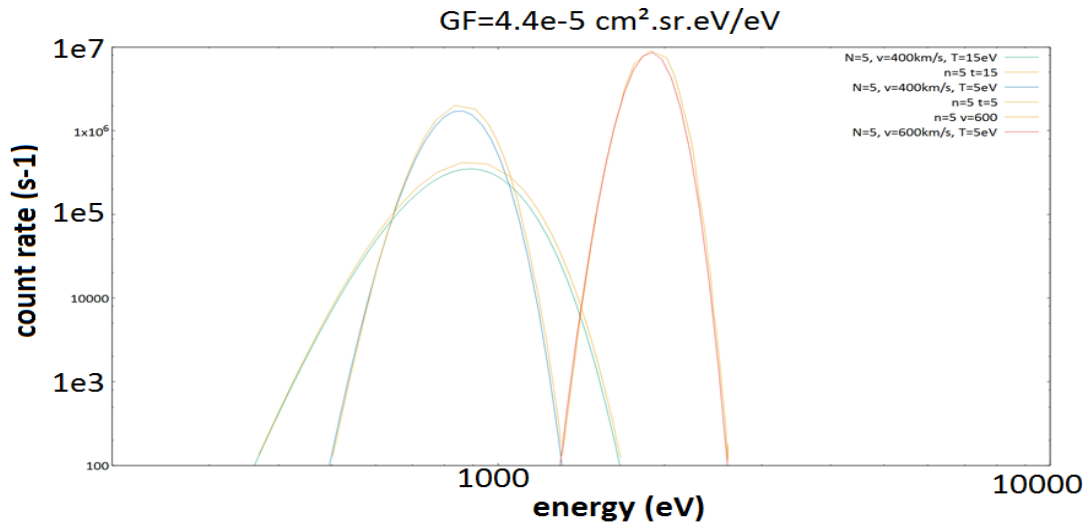
337

$$f(v) = N \cdot \left(\frac{m}{2\pi \cdot k_B \cdot T} \right)^{\frac{3}{2}} \cdot e^{-\left[\frac{v-v_0}{v_{th}} \right]^2} \quad \text{with N the density and T the temperature,} \quad v_{th} = \sqrt{\frac{2 \cdot kT}{m}} \quad (3.1)$$

338 Then the count rate measured by the instrument is related to the distribution function
 339 through the geometric factor (with τ the elementary acquisition time) as follows:

$$C = f(\vec{E}) \cdot \frac{2\tau \cdot E_0^2}{m^2} \cdot \text{GF}_{ijk} = f(\vec{v}) \cdot \frac{\tau \cdot v_0^4}{2} \cdot \text{GF}_{ijk} \quad (3.2)$$

340 Figure 11 shows the count rate estimated for different types of solar wind, according to
 341 their density, speed and temperature. Three sets of values are used in Figure 11, with speeds of
 342 400 and 600 km/s and temperatures of 15 and 5 eV, respectively for the slow and fast solar winds.
 343 An unusual case of hot (15 eV) and slow (400 km/s) solar wind is also shown for context. A typical
 344 density of 5 cm^{-3} is used in all cases. The maximal count rate for a 3° bin is near 10^7 count/s for a
 345 fast solar wind, which is essentially the saturation level of one CEM. By using 32 CEMs over the
 346 $\pm 24^\circ$ FOV, our proposed design thus diminishes this saturation by a factor 2, and at the same
 347 time increase the azimuth angular resolution to 1.5° .



348

349 Figure 11. Count rate estimated for a 3° azimuthal angular sector in the present design. There are curves for 3 types
 350 of solar wind: typical slow ($T = 5 \text{ eV}$ and $V = 400 \text{ km/s}$) and fast ($T = 15 \text{ eV}$ and $V = 600 \text{ km/s}$) winds, as well as a
 351 very unusually hot and slow wind for context ($T = 15 \text{ eV}$ and $V = 400 \text{ km/s}$). For each type of wind, the count rates
 352 have been estimated using both Simion and Trace simulations.

353

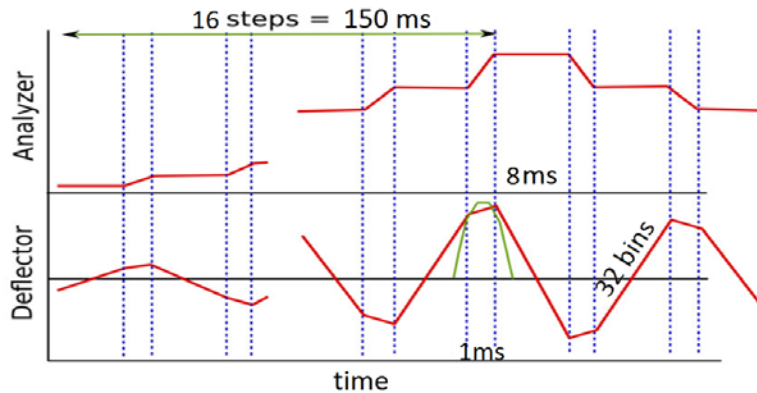
354 3.2 Measurement scheme

355 The next aspect of the present study deals with the choice of the energy-elevation stepping
356 scheme and its impact on the accumulated counts measured by the instrument. As mentioned
357 previously, one of the science requirements is to obtain a full 3D distribution function in 150 ms.
358 This measurement should be done with as many energies and elevations as possible, for science
359 purposes, but this directly impacts the elementary accumulation time and thus the accumulated
360 counts per bin. A trade-off must be found to obtain high time, energy, and angular resolutions,
361 together with a good coverage of the 3D distribution and a good statistic.

362 For that purpose the instrument design should use 96 basic energy bins of 7% each over a
363 range of order 20 eV – 20 keV. Because the solar wind is a cold beam of variable peak energy
364 (corresponding to the solar wind bulk speed), a beam tracking strategy will be implemented in
365 order to focus the measurements only on the energy range where significant flux is present (e.g.,
366 Figure 11). Several modes will be implemented in order to measure solar wind beams of variable
367 temperatures, and some modes will be devised in order to measure both protons and alphas (with
368 16, 24, 32, or 46 energy bins, for instance).

369 To exemplify the measurement scheme only 16 steps in energy (and 32 elevation) is
370 considered here. The corresponding chronogram is represented in Figure 12. Within each of the
371 16 steps in energy, the deflector voltages are swept linearly (cf. Figure 8) in order to cover the
372 required elevation range. The full deflection can typically be divided into 16 or 32 basic elevation
373 bins (3° or 1.5°), and appropriate counters are implemented in the FPGA using the baseline
374 accumulation time.

375



376

377 Figure 12. Chronogram with 16 steps in energy and 32 elevation bins. The highest energy step shown after the 150
378 ms arrow is only meant to show that the next sweep in energy may have a different energy range owing to the
379 requirement for energy tracking of the solar wind proton beam (but this is not discussed in details in the present paper).
380 Note also that adjacent energy sweeps may be done in successive ascending / descending order so as to avoid dead
381 times required for setting back the high voltages to low values.

382

383 3.3 Detailed scientific performance

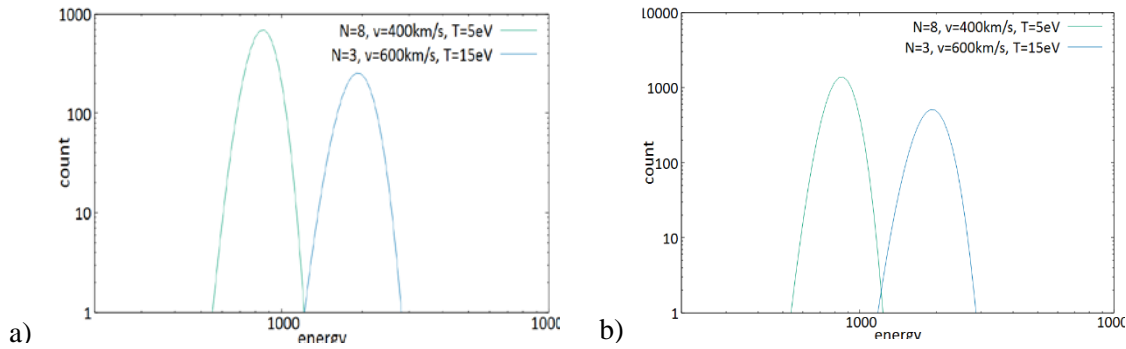
384 The statistic is given by the accumulated counts:

385

$$C_{acq} = f(\vec{E}) \cdot \frac{2 \cdot E_0^2}{m^2} \cdot \mathbb{G} \mathbb{F}_{ijk} \cdot \frac{T_{3D}}{n_{step_E} \cdot n_{step_{el}}} \quad (3.3)$$

386 The counts that would be observed as a function of energy with the present instrument
 387 design are displayed in Figure 13 for two angular resolutions and solar wind properties (slow and
 388 fast solar winds). Figure 13a shows the counts expected for 16 steps in energy and the highest
 389 angular resolution (32 elevations and azimuths of 1.5° each). As can be seen, the statistics is
 390 reasonably high for such typical solar wind densities. In cases of tenuous solar wind (e.g., 1 cm^{-3}),
 391 the statistics can be increased by a factor 4 by summing angular bins 2×2 so that the distribution
 392 function is now made up of 16 elevations and azimuths of 3° each. The statistics obtained by such
 393 a summation process is illustrated in Figure 13b.

394

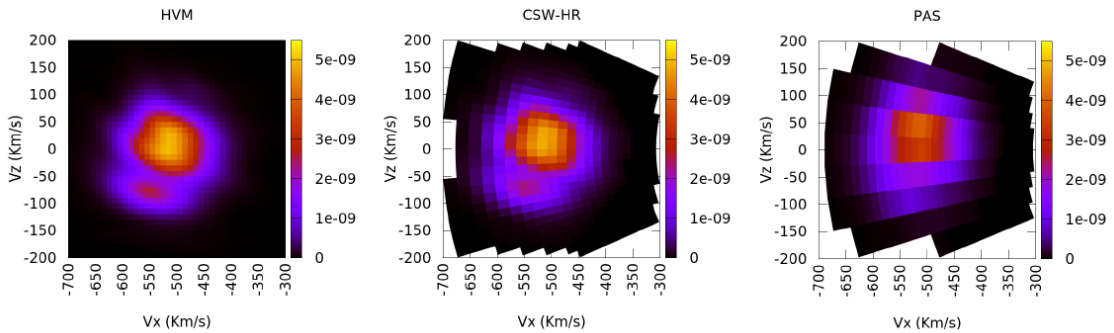


395 Figure 13. Accumulated counts estimated for a 16 energy step mode with (a) 1.5° and (b) 3° angular bins.

396

397 The unprecedented high resolution measurements that are expected from this design are
 398 illustrated in Figure 14. Figure 14a shows the proton velocity distribution from a Hybrid Vlasov-
 399 Maxwell simulation [Valentini et al., 2007] of solar-wind turbulence [Servidio et al., 2012; 2015;
 400 Valentini et al., 2014], displaying a complex structure in velocity space with the presence of a
 401 marked particle beam. The corresponding observations expected for the present design (THOR
 402 CSW) and the PAS instrument on Solar Orbiter are respectively shown in Figures 14b and 14c
 403 (here the solar wind bulk speed is 500 km/s). This figure highlights the capability of this design to
 404 isolate fine structures in the distribution function such as faint suprathermal beams (cf. also
 405 DeMarco et al. [2016]).

406



407

408 Figure 14. Illustration of the expected measurements of the proton distribution function on the basis of solar wind
409 simulations described in *DeMarco et al.* [2016], respectively for the properties of (a) the simulation itself [*Valentini*
410 *et al.*, 2007], (b) the present design (THOR CSW instrument), and (c) the Solar Orbiter PAS instrument. The data is
411 represented in a system equivalent to Geocentric Solar Ecliptic (GSE) coordinates.

412

413 3.4 Additional comments

414 The proposed measurement scheme leads to high constraints for the electronic system of
415 CSW. For instance, the slew rate of the deflector power supplies must be higher than 500 V/ms to
416 measure the 2D distribution of 20 keV particle within 8 ms (cf. Figure 12), but this is achievable
417 with current HV systems. The front-end electronics also is a key for instrument performance. The
418 electronic front-end must be able to detect particles with count rate close to CEM saturation ($\sim 10^7$
419 c/s). For that purpose, a multi-channel ASIC (Application Specific Intergrated Circuit) is currently
420 being designed. The FPGA counters also must be efficient enough to register all counts from the
421 front-end.

422 Finally, the amount of data resulting from such a high resolution (time, energy and angle)
423 measurement scheme is very large (~ 1800 kbits/s or more). Although the instrument will be
424 continuously operating in burst mode, the telemetry is not sufficient to downlink all data in burst.
425 Burst data will thus only be downlinked in selected location using a “Scientist In The Loop” (SITL)
426 system akin to that used for the Magnetospheric Multiscale (MMS) mission [*Baker et al.*, 2016;
427 *Fuselier et al.*, 2016; *Phan et al.*, 2016]. All these additional aspects are currently being studied
428 and will be reported in future communications.

429

430 4. Conclusions

431 This paper described an instrument design that permits unprecedentedly accurate
432 measurements of the solar wind proton beam with high temporal, energy and angular resolutions.
433 These properties fulfill the requirements of the THOR mission, which aims at addressing
434 collisionless turbulence in space plasmas. We first described the mechanical design of the
435 proposed instrument. It is composed of a top-hat electrostatic analyzer for incident particle energy-
436 per-charge selection, a collimator at its entrance for obtaining the appropriate high energy
437 resolution, as well as deflectors for the elevation angle selection. A first analysis showed that
438 microchannel plates (MCP) cannot be used because of their low count rate saturation. Instead,
439 channel electron multipliers (CEM) were chosen. Simulations were performed to define an
440 appropriate electrostatic analyzer. It was designed to have an analyzer constant K of 13.8, an
441 energy resolution of 7%, an elevation resolution of 1.7° and a transmission rate (geometric factor)
442 of $4.4 \times 10^{-5} \text{ cm}^2 \cdot \text{sr} \cdot \text{eV}/\text{eV}$ for 3° azimuthal bins. Deflectors were also designed through
443 simulations to optimize the applied voltages, FOV, and angular resolution. The simulations show
444 a deflector efficiency of $132^\circ \cdot \text{V}/\text{V}$ for an elevation range larger than $\pm 25^\circ$, thus fulfilling the
445 FOV requirements. Finally, the CSW response has been studied for typical solar wind conditions
446 assuming Maxwellian distribution functions. With the proposed design, the count rate is about 10^7
447 count/s. This is consistent with the choice of CEMs as detectors, instead of MCPs, to avoid
448 saturation. To further decrease the chance of saturation and at the same time increase the angular
449 resolution by a factor 2, we decided to design the instrument with 32 CEMs covering 1.5° each
450 over the $\pm 24^\circ$ azimuthal FOV. In summary, thanks to its high geometric factor and 32 CEMs,
451 this design will provide the THOR CSW instrument with unprecedentedly fast (150 ms) and high

452 angular (1.5°) resolution measurements of the solar wind protons and alphas. A direct comparison
453 with realistic simulations of turbulent plasmas reveals that the proposed instrumentation will be
454 crucial for the description of the fine dynamics of the solar wind.

455

456 Acknowledgments

457 Work at IRAP was supported by CNRS and CNES. We also acknowledge support from
458 the SME EREMS in Flourens, France. Work at IASB-BIRA was supported by PRODEX THOR-
459 CSW Development PEA 4000116805. Work at University of Calabria, Italy and at IAPS/INAF,
460 Rome, has been supported by the Agenzia Spaziale Italiana under the Contract No. ASI-INAF
461 2015-039-R.O “Missione M4 di ESA: Partecipazione Italiana alla fase di assessment della
462 missione THOR.”

463

464 References

465 Baker, D. N., L. Riesberg, C. K. Pankratz, R. S. Panneton, B. L. Giles, F. D. Wilder, and R. E.
466 Ergun (2016), Magnetospheric Multiscale Instrument Suite Operations and Data System, Space
467 Sci. Rev., 199, 1-4, 545-575.

468 Bruno, R., and V. Carbone (2013), The Solar Wind as a Turbulence Laboratory. Living Reviews
469 in Solar Physics, 10:2.

470 Carlon, C. W., and J. P. McFadden (1998), Design and application of imaging plasma instruments,
471 Measurement Techniques in Space Plasmas: Particles, Geophysical Monograph 102, American
472 Geophysical Union.

473 Carlson C.W., et al. (1982), An Instrument for Rapidly Measuring Plasma Distribution
474 Functions with High Resolution, Adv. Space Res., 2, 7, 67.

475 Collinson, G. A. (2012), The geometric factor of electrostatic plasma analyzers: A case study from
476 the Fast Plasma Investigation for the Magnetospheric Multiscale mission, Rev. Sci. Instrum., 83,
477 033303

478 De Marco, R., M. F. Marcucci, R. Bruno, R. D'Amicis, S. Servidio, F. Valentini, B. Lavraud, P.
480 Louarn, and M. Salatti (2016), Importance of energy and angular resolutions in top-hat
481 electrostatic analysers for solar wind proton measurements, J. Instrum., 11, 08, C08010.

482 Fedorov, A., et al. (2004), Internal report of STEREO Solar Wind Electron Analyzer (SWEA)
483 calibrations, Institut de Recherche en Astrophysique et Planétologie, Toulouse, France.

484 Fuselier, S. A., W. S. Lewis, C. Schiff, R. Ergun, J. L. Burch, S. M. Petrinec, and K. J. Trattner
485 (2016), Magnetospheric Multiscale Science Mission Profile and Operations, Space Sci. Rev., 199,
486 1-4, 77-103.

487 Kasper, J. C., et al. (2016), Solar Wind Electrons Alphas and Protons (SWEAP) Investigation:
488 Design of the solar wind and coronal plasma instrument suite for Solar Probe Plus, *Space Sci.*
489 *Rev.*, submitted.

490 Lin, R. P., et al. (1995), A three-dimensional plasma and energetic particle investigation for the
491 wind spacecraft, *Space Sci. Rev.*, 71, 1, 125–153.

492 Marsch, E. (2006), Kinetic Physics of the Solar Corona and Solar Wind, *Living Rev. Solar Phys.*,
493 3, 1.

494 McComas, D. J., S. J. Bame, P. Barker, W. C. Feldman, J. L. Phillips, P. Riley, and J. W. Griffiee
495 (1998), Solar Wind Electron Proton Alpha Monitor (SWEAPAM) for the Advanced Composition
496 Explorer, *Space. Sci. Rev.*, 86, 1, 563–612.

497 Montgomery, M. D., S. P. Gary, D. W. Forslund, and W. C. Feldman (1975), Electromagnetic ion-
498 beam instabilities in the solar wind, *Phy. Rev. Lett.*, 35, 667-670.

499 Phan, T. D., M. A. Shay, J. P. Eastwood, V. Angelopoulos, M. Oieroset, M. Oka, and M. Fujimoto
500 (2016), Establishing the Context for Reconnection Diffusion Region Encounters and Strategies for
501 the Capture and Transmission of Diffusion Region Burst Data by MMS, *Space Sci. Rev.*, 199, 1-
502 4, 631-650.

503 Pollock, C., et al. (2016), Fast Plasma Investigation for Magnetospheric Multiscale, *Space Sci.*
504 *Rev.*, DOI: 10.1007/s11214-016-0245-4.

505 Ogilvie, K. W., et al. (1995), SWE, a comprehensive plasma instrument for the WIND
506 spacecraft, *Space Sci. Rev.*, 71, 55.

507

508 Rème, H., et al. (2001), First multispacecraft ion measurements in and near the earth's
509 magnetosphere with the identical CLUSTER Ion Spectrometry (CIS) Experiment, *Ann. Geophys.*,
510 19, 10-12, 1303-1354.

511 Schwartz, S. J., et al. (2009), Cross-scale: multi-scale coupling in space plasmas, *Exp. Astr.*, 23,
512 1001-1015.

513 Servidio, S., F. Valentini, F. Califano, P. Veltri, Local Kinetic Effects in Two-Dimensional Plasma
514 Turbulence, *Phys. Rev. Lett.* 108, 045001 (2012)

515 Servidio, S., F. Valentini, D. Perrone, A. Greco, F. Califano, W. H. Matthaeus and P. Veltri, A
516 kinetic model of plasma turbulence, *J. Plasma Physics* 81, 325810107 (2015)

517 Vaivads, A., A. Retinò, J. Soucek, Yu. V. Khotyaintsev, F. Valentini, C. P. Escoubet, O.
518 Alexandrova, M. André, S. D. Bale, M. Balikhin, D. Burgess, E. Camporeale, D. Caprioli, C. H.
519 K. Chen, E. Clacey, C. M. Cully, J. De Keyser, J. P. Eastwood, A. N. Fazakerley, S. Eriksson, M.
520 L. Goldstein, D. Graham, S. Haaland, M. Hoshino, H. Ji, H. Karimabadi, H. Kucharek, B. Lavraud,
521 F. Marcucci, W. H. Matthaeus, T. E. Moore, R. Nakamura, Y. Narita, Z. Nemecek, C. Norgren,
522 H. Opgenoorth, M. Palmroth, D. Perrone, J.-L. Pinçon, P. Rathsman, H. Rothkaehl, F. Sahraoui,
523 S. Servidio, L. Sorriso-Valvo, R. Vainio, Z. Vörös, and R. F. Wimmer-Schweingruber (2016),

524 Turbulence Heating ObserveR - satellite mission proposal, *J. Plas. Phys.*, 82, 5, doi:
525 10.1017/S0022377816000775.

526 Valentini, F., P. Travnicek, F. Califano, P. Hellinger, A. Mangeney, A hybrid-Vlasov model based
527 on the current advance method for the simulation of collisionless magnetized plasma, *J. Comput.*
528 *Phys.* 225, 753 (2007)

529 Valentini, F., S. Servidio, D. Perrone, F. Califano, W. H. Matthaeus, and P. Veltri, Hybrid Vlasov-
530 Maxwell simulations of two-dimensional turbulence in plasmas, *Phys. Plasmas* 21, 082307 (2014)

531